Y. Xu a, B. Ding B. Wu b,*

^a College of Materials Science and Engineering, Key Laboratory of New Processing Technology for Nonferrous Metals and Materials, Ministry of Education, Guilin University of Technology, Guilin 541004, China
^b Guangxi Technological College of Machinery and Electricity, Nanning 530007, China

The selective electrooxidation of benzyl alcohol (BA) to benzoic acid (BAC) requires the development of efficient and cost-optimized electrocatalysts. Herein, cobalt-vanadium layered double hydroxide (CoV-LDH) was prepared by co-precipitation, and subsequently transformed into cobalt-vanadium bimetallic phosphides (P-CoV) through a topological transformation process using sodium hypophosphite as the phosphorus source. Structural and morphological analyses revealed that P-CoV retained the two-dimensional layered architecture of the CoV-LDH precursor, offering more electrochemically active surface area and enhancing electronic conductivity. Electrochemical evaluation demonstrated that under the optimal conditions (initial potential of 0.5 V vs. Ag/AgCl at 25°C), P-CoV achieved a BA conversion of 61.60% and a BAC selectivity of 82.67% for 9 h. These results highlight the promising application of non-noble metal bimetallic phosphides in the energy-efficient and selective electrooxidation of aromatic alcohols under mild operating conditions.

(Received July 2, 2025; Accepted October 13, 2025)

Keywords: Bimetallic phosphide, Layered double hydroxide, Topological transformation, Electrocatalysis, Benzyl alcohol oxidation

1. Introduction

As important fine chemicals, benzaldehyde (BAD) and benzoic acid (BAC) are ubiquitously used in the fields of food, medicine, and fragrance industries. However, traditional synthetic methods, such as liquid-phase oxidation of toluene or hydrolysis of benzyl chloride, are often associated with drawbacks including low yield, complex process, equipment corrosion and environmental pollution [1]. In recent years, electrocatalytic oxidation of benzyl alcohol (BA) has emerged as a promising green alternative, offering mild reaction conditions, high selectivity, and the elimination of the need for external oxidants [2]. To date, various electrocatalyst systems have been developed for the reaction, primarily classified as materials based on transition metals and those based on noble metals. Precious metal catalysts, for example Ir-, Au-, and Pd-based systems (e.g., Au/Pd/TiO₂), can achieve high BA conversion rates (~80%), but suffer from high cost and limited availability, restricting their practical scalability [3]. In contrast, transition metal-based materials, such as hydroxides supported on nickel-foam, offer low-cost alternatives and have achieved impressive conversion rates (~95%) [4]. However, these systems often exhibit limited compositional tunability and structural instability, restricting their long-term electrocatalytic performance. To overcome these limitations, it is imperative to explore the synthesis of non-noble metal-based electrocatalysts that exhibit both adequate performance and structural stability.

The conductive properties similar to those of metals and the high catalytic activity exhibited by transition metal phosphides (TMPs) make them regarded as ideal electrocatalytic materials [5]. The incorporation of phosphorus atoms into metal lattice alters the electronic structure by expanding interatomic distances, weakening metal—metal interactions, and shifting the d-band center, all of which optimize the sorption-desorption behavior of reaction intermediates [6]. These effects contribute to enhanced charge transfer and overall catalytic performance. While monometallic TMPs

^{*} Corresponding author: prometheus330@qq.com https://doi.org/10.15251/DJNB.2025.204.1285

(such as NiP [7], CoP [8], MoP [9]) have demonstrated their functions and kinetics are often affected by limitations of their active sites. In contrast, bimetallic or multimetallic TMPs benefit from synergistic effects between different metal centers, which can optimize the electronic structure [10, 11], enrich the density of catalytic sites, and promote charge transport. Despite these advantages, many existing polymetallic TMPs still face challenges such as activity degradation and poor selectivity in alkaline conditions [12].

Layered double hydroxides (LDHs) are generally considered to be 2D materials with the molecular formula $[M^{2+}_{1-x}M^{3+}_{x}(OH)_{2}](A^{n-})_{x/n} \cdot mH_{2}O$ [13], which possesses adjustable laminate M^{2+}/M^{3+} composition and interlayer anion-exchange capability, representing an ideal platform for the construction of polymetallic phosphide [14]. The incorporation of heteroatoms such as V, Fe, or Ni can further tailor their electronic and catalytic properties [15]. During the phosphating process, the topological conversion of LDHs can yield layered TMPs with well-preserved morphology, high electrochemical surface area, and enriched active sites [16, 17].

Herein, we introduce the synthesis of a cobalt–vanadium bimetallic phosphide (P-CoV) via topological transformation of CoV-LDH using sodium hypophosphite (NaH₂PO₂) as a phosphorus source. The resulting P-CoV catalyst maintained a layered architecture with fully exposed active sites and high electron conductivity. Electrochemical testing revealed that P-CoV achieved a BA conversion of 61.60% and a BAC selectivity of 82.67% at 25°C with an initial potential of 0.5 V (vs. Ag/AgCl) over a catalytic process of 9 h. All findings demonstrate the potential of LDH-derived bimetallic phosphides as efficient, cost-effective, and stable electrocatalysts for aromatic alcohol oxidation.

2. Experimental

2.1. Materials

NaOH, KOH, CoCl₂·6H₂O, and NaNO₃ were bought from Xilong Chemical Reagent Co., Ltd. VCl₃, Formamide, benzoic acid (BAC), and benzaldehyde (BAD) were sourced from Aladdin Biochemistry Technology (Shanghai, China) Co., Ltd. Benzyl alcohol (BA, 99%), and NaH₂PO₂ were bought from Rhawn chemical reagent Co., Ltd. Nickel foam (NF) was supplied by Changde Liyuan New Material Co., Ltd. All aforementioned pharmaceuticals were used as received, without undergoing additional processing.

2.2. Characterizations

X-ray powder diffraction (XRD) patterns were analyzed by X' Pert PROX using a Cu Ka radiation source (λ = 1.5405 Å). Fourier transform infrared spectroscopy (FT-IR) spectra (4000-500 cm⁻¹) were characterized by using a Thermo Nicolet NEXUS 670 spectrometer. The morphologies and microstructures of the samples were examined by scanning electron microscope (SEM, Hitachi S-4800). The energy dispersive X-ray spectrum (EDS) was analyzed by using the X-ray energy dispersive spectrometer attached to the scanning electron microscope.

2.3. Synthesis of CoV-LDH, CoV-LDO, and P-CoV

CoV-LDH was prepared by coprecipitation method [18]. A 10.0 mL solution containing CoCl₂·6H₂O (0.03 M) and VCl₃ (0.01 M) was slowly added dropwise into another substrate comprising 10.0 mL of NaNO₃ (0.01 M) and 23 vol% formamide. Meanwhile, under magnetic stirring at 80°C, 0.15 M NaOH solution was dropped in to maintain the pH value at around 12. The entire process was finished within 10 min. Subsequent to this, a centrifugal washing process was employed on the suspension, and the precipitate was repeatedly washed by deionized water until the pH became neutral, after being dried at 60°C until a constant weight was achieved, CoV-LDH was obtained. With CoV-LDH powder being calcined in a porcelain boat under Atmosphere, CoV-LDO is successfully made. heating rate of 2°C/min under 20°C-350°C, hold at 350°C for 2 h, cooling in air to room temperature.

The preparation of the P-CoV was carried out through a topological transformation of CoV-LDH. In a conventional procedure, 0.3 g CoV-LDH and 2.64 g NaH₂PO₂ were evenly distributed in separate quartz porcelain boats and placed 2 cm apart in a tubular furnace. Specifically, NaH₂PO₂

was positioned at the upstream inlet, while CoV-LDH was placed downstream (outlet side), opposite to the phosphorus source. Subsequently, the samples were subjected to annealing under Ar atmosphere at the temperature of 350°C for a duration of 2 h with the heating rate of 2°C /min. The resulting black powder product, denoted as P-CoV, was collected for further characterization.

2.4. Electrochemical measurements

Successive electrochemical performance detections were conducted in 1.0 M KOH solution and a mixed electrolyte constituted by 1.0 M KOH & 10 mM BA, which corresponded to OER activity & BA electrooxidation evaluation in the respective situations. The experiment was conducted using a conventional three-electrode system equipped with a CHI-660 electrochemical detection device. In this system, NF-supported CoV-LDH, CoV-LDO, and P-CoV were successively used as the working electrodes, using the Ag/AgCl electrode as the reference electrode and the Pt sheet (1.5×1.5 cm²) as the counter electrode. The conversion of the measured potential vs. Ag/AgCl to a reversible hydrogen electrode (RHE) scale was conducted in accordance with the Nernst equation: $E_{RHE} = E_{Ag/AgCl} + 0.059 \text{ pH} + 0.197 [19]$. Cyclic voltammetry (CV) tests were performed between 0-0.7 V at a scan rate of 50 mV/s, scanning segments was set to 20. The LSV curves were obtained with a scan rate of 5 mV/s for the potential interval of 0-0.1 V. The electrochemical impedance spectroscopy (EIS) was completed under the potential of 0.5 V within the frequency of 100 k-0.01 Hz, while the electrochemical surface area (ECSA) is evaluated by analyzing the CV curve under different scanning speeds from 0.03 V to 0.34 V. The scanning speed is set as 2, 4, 6, 8, 10 mV/s. The formula is also used to calculate ECSA: ECSA = C_{dl}/C_s (where C_{dl} (double-layer capacitance) is the slope of the CV curve and C_s is the specific capacitance of the sample).

2.5. Electrooxidation of benzyl alcohol

The electrooxidation was carried out with a chronoamperometry (i–t) technique. The same three-electrode configuration used for electrochemical measurements is employed here. The anode compartment contained 10mM BA dissolved in KOH (1.0 M), while the cathode was filled with 1.0 M KOH solution. The electrocatalysis reaction was executed constantly at current for 9 h. At every 1 h interval, 1mL of the reaction solution was slowly pulled out and mixed immediately with 1 mL of 1M HCl solution so that the pH could be neutralized to around 7.0 for subsequent examination of the products under control conditions. Used HPLC, Therm Fisher U3000 coupling ultraviolet detector and C18(2) column for the quantitative analysis of BA and its oxidation products. The mobile phase used in this experiment was distilled water and acetonitrile with a volume ratio of H₂O/CH₃CN=1. A flow rate of 1 mL/min was used. The calculation of BA (C_{BA}) conversion rate and its oxidative product selectivity are carried out according to the following equations:

$$C_{BA}(\%) = \frac{c_{BA}^0 - c_{BA}^t}{c_{BA}^0} \times 100\%$$
 (1)

$$S_{BAC}(\%) = \frac{c_{BAC}}{c_{BAC} + c_{BAD}} \times 100\%$$
 (2)

$$S_{BAD}(\%) = \frac{c_{BAD}}{c_{BAC} + c_{BAD}} \times 100\%$$
 (3)

where C_{BA}^{0} and C_{BA}^{t} are respectively represent concentrations of BA at initial and various detection times, C_{M} represent the concentrations of the catalytic products (M = benzoic acid (BAC), benzaldehyde (BAD)) at different reaction times [20].

3. Results and discussion

X-ray diffraction (XRD) patterns for the crystal structures of CoV-LDH, CoV-LDO and P-CoV are shown in Fig. 1a. The XRD result of CoV-LDH showed that the Bragg diffraction peaks were located at 11.58°, 23.41°, 35.11°, 46.23°, and 59.08°, respectively. This observation is in

accordance with the (003), (006), (009), and (110) crystal planes that are characteristic of a typical LDH structure [21]. The successful synthesis of CoV-LDH is therefore confirmed. After calcination of CoV-LDH under the protection of Ar atmosphere, the resulting CoV-LDO sample displayed the characteristic diffraction peaks matching well with those of Co₃O₄, indicating that Co₃O₄ might be the dominant crystalline phase [22]. The idea is that replacing some Co atoms with V causes the appearance of oxygen vacancy, which leads to the increasing activity sites density and favors reactants molecules' adsorption and dissociation. The characteristic diffraction peaks in the XRD spectrum of P-CoV correspond to the orthorhombic CoP, indicating that CoP is the dominant crystalline phase. The incorporation of V into the CoP lattice is expected to modulate the affinity selection of reaction intermediates, thereby favoring the selective oxidation of BA to BAC rather than overoxidation to CO2. FT-IR spectra (Fig. 1b) of CoV-LDH, CoV-LDO and P-CoV provide further insight into the structural evolution during the synthetic process. For CoV-LDH, the broad band present in the range around 3650-2950 cm⁻¹ is mainly due to the O-H stretch and intercalated water molecules. 1650 cm⁻¹ absorption peak is for inter-layer water molecule bending vibration, 1350 cm⁻¹ absorption for inter-layer anion CO₃². Absorption peaks below 1000 cm⁻¹ are indicative of metal-oxygen (M-O) vibrations. In contrast, FT-IR spectra of CoV-LDO and P-CoV show weakened or absent peaks within the range of 1620-1400 cm⁻¹, suggesting that the progressive removal of interlayer water molecules, O-H, and CO₃² of CoV-LDH during the processes of calcination and phosphating.

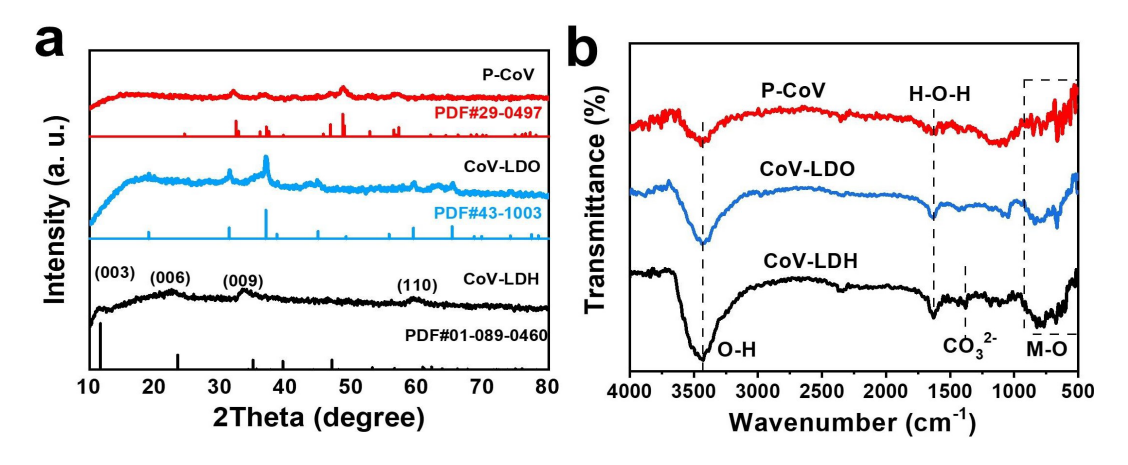


Fig. 1. (a) XRD patterns and (b) FT-IR spectra of CoV-LDH, CoV-LDO, and P-CoV.

Surface features and microstructural characteristics of the catalysts were examined using scanning electron microscopy (SEM) coupled with energy-dispersive X-ray spectroscopy (EDS). As demonstrated in Fig. 2a. CoV-LDH precursor exhibited a layered structure consisting of stacked nano-lamellas. The corresponding EDS spectrum (Fig. 2b) revealed the elemental composition of CoV-LDH as C: 48.22%, O: 33.81%, Co: 13.66%, and V: 4.31%, with a Co:V atomic ratio of 3.17:1.00. This ratio is close to the feeding ratio, confirming the reliability and reproducibility of the co-precipitation method for precursor synthesis. After thermal treatment under an inert atmosphere, the CoV-LDO sample showed partial structural collapse, with a significant loss of the original layered architecture (Fig. 2c). EDS analysis (Fig. 2d) showed the increase content of C element, likely due to residual carbonaceous species or changes during calcination. In contrast, the P-CoV sample (Fig. 2e) retains the lamellar nanosheet morphology, indicating good structural stability after phosphating. The retained lamellar structure has fully exposed catalytic sites and a large specific surface area, further increasing the catalytic ability. EDS elemental mapping (Fig. 2e) showed a substantial increase in phosphorus content, confirming the successful incorporation of phosphate species. Furthermore, the ratio of metal-to-phosphorus was close to 1:1, suggesting the formation of conductive metal phosphide phases, which is favorable for maintaining good electrical conductivity in electrocatalytic applications.

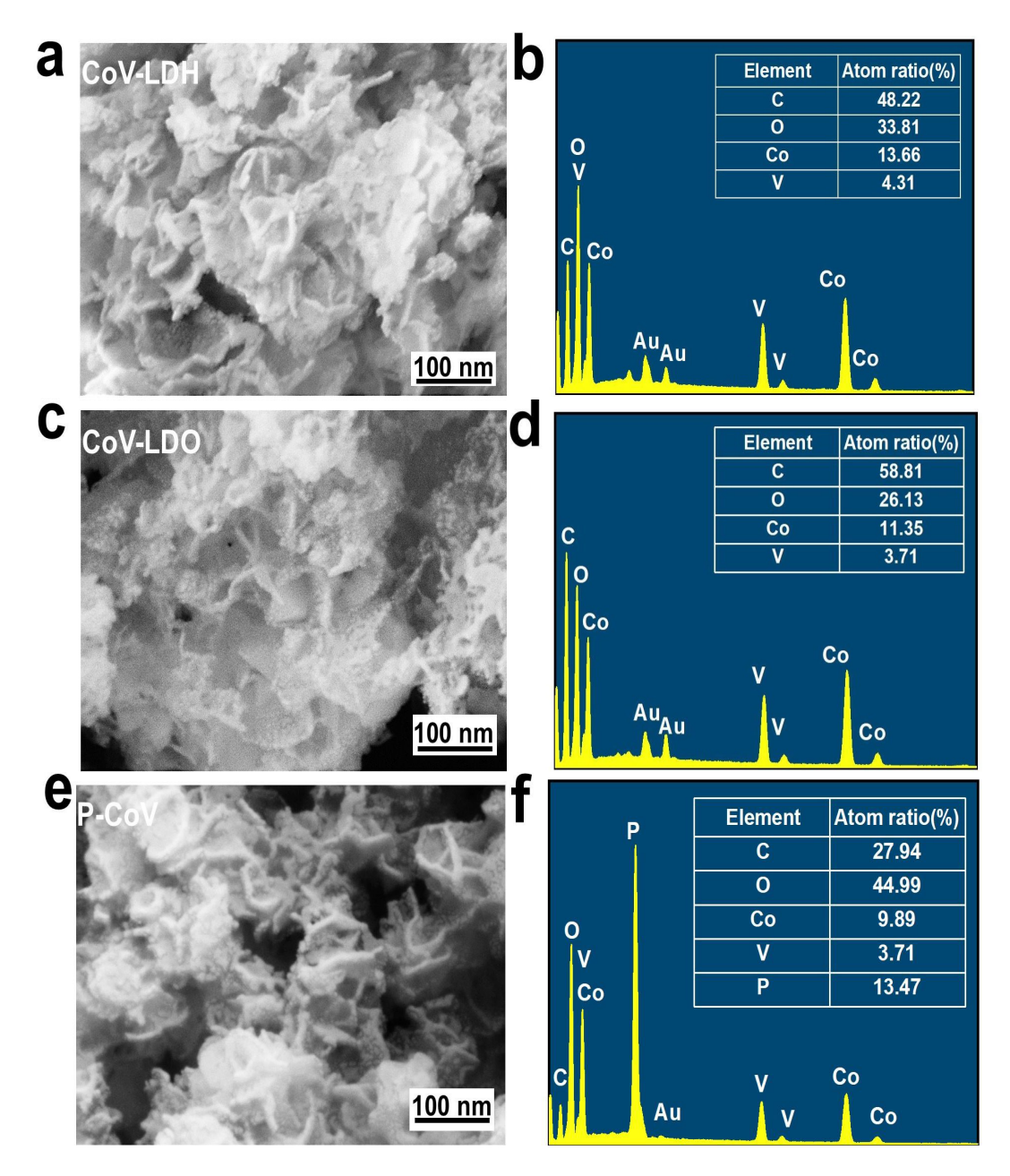


Fig. 2. SEM images of (a) CoV-LDH, (c) CoV-LDO, and (e) P-CoV; EDS spectra of (b) CoV-LDH, (d) CoV-LDO, and (f) P-CoV.

In an aqueous environment, BA electrooxidation frequently competes with OER, which could impede the entire catalytic process. In order to differentiate between the two processes, electrochemical tests were performed step by step in 1.0M KOH solution (OER activity), and the mixed solution of 1.0M KOH + 10mM BA (BA electro-oxidization activity). As shown in the cyclic voltammetry (CV) curves in Fig. 3a, P-CoV exhibited a significantly higher peak current density compared to CoV-LDH and CoV-LDO, indicating superior OER performance. Moreover, in the BA-containing electrolyte (Fig. 3d), P-CoV demonstrated a marked increase in peak current density, while CoV-LDH and CoV-LDO showed negligible change. This enhancement demonstrated that P-CoV possesses higher electrocatalytic activity for BA than for OER activity. LSV curves (Fig. 3b) indicated that P-CoV achieved a current density of 100 mA/cm² at a notably lower potential of 1.73 V (V vs. RHE) compared to CoV-LDO and CoV-LDH, indicating its superior OER activity. Similar trends were observed in the BA-containing electrolyte (Fig. 3e), reaffirming that P-CoV exhibits enhanced catalytic activity toward BA electrooxidation. The kinetics of electrode reactions can be

evaluated by charge transfer resistance (Rct). Its value is represented by the semicircle in the Nyquist plot analyzed by EIS. A smaller semicircle indicates a faster reaction speed. The equivalent circuit diagram illustrates the electrolyte resistance (Rs) and Rct, where Rs is the electrolyte resistance of the electrochemical reaction. Fig. 3c shows that P-CoV displays the smallest radius in electrolyte with only KOH, indicating the smallest charge transfer resistance and the fastest electron transfer kinetics among the three samples. This trend was also observed in the mixed electrolyte (Fig. 3f). The corresponding fitted equivalent circuit diagrams further distinguished the R_s and R_{ct}, highlighting the superior conductivity and charge transfer performance of P-CoV. These results suggest the exceptional catalytic performance exhibited by P-CoV may stem from its unique conformation and phosphorus doping.

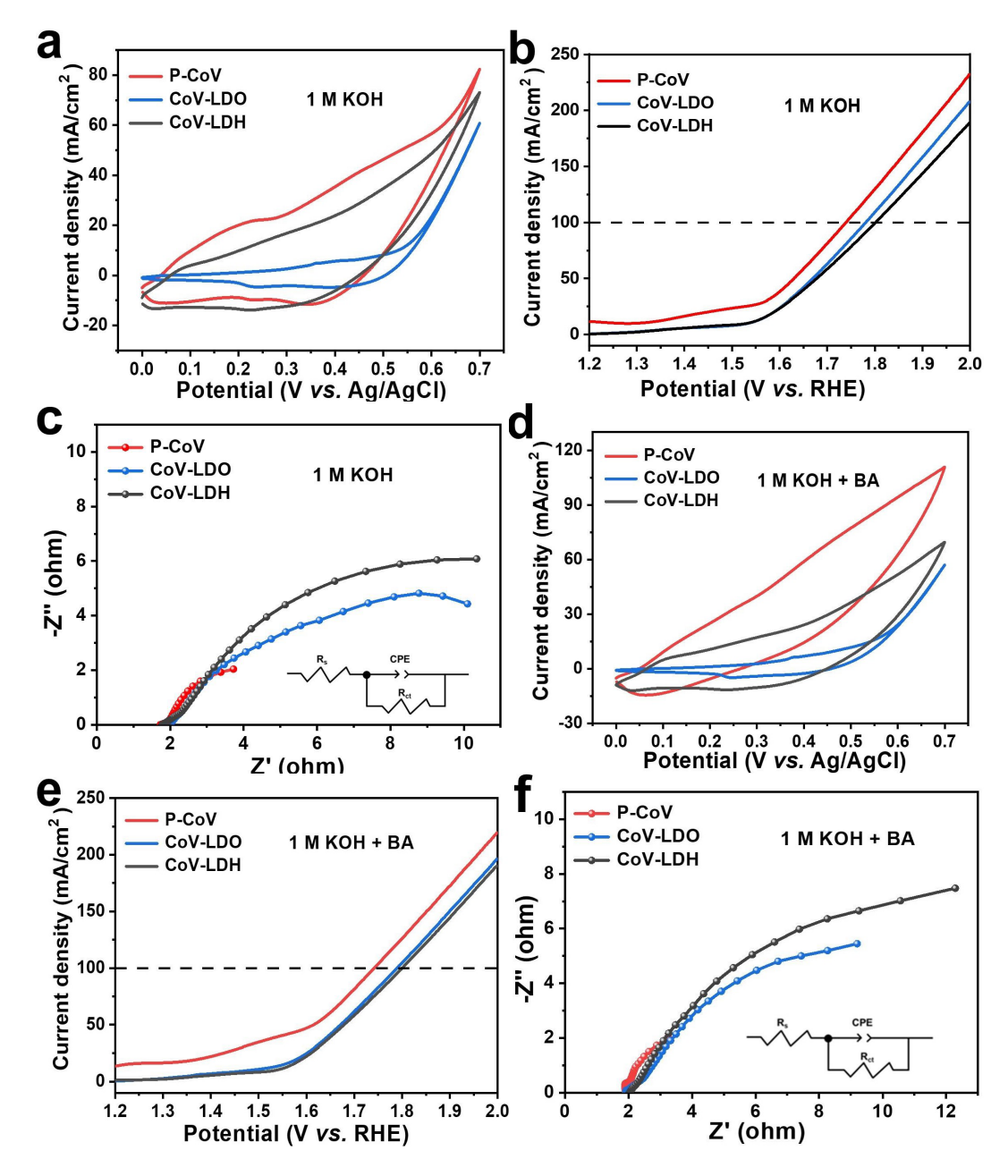


Fig. 3. (a) CV curves, (b) LSV curves, and (c) Nyquist plots of CoV-LDH, CoV-LDO, and P-CoV in 1.0 M KOH. (d) CV curves, (e) LSV curves, and (f) Nyquist plots of CoV-LDH, CoV-LDO, and P-CoV in 1.0 M KOH with 10 mM BA.

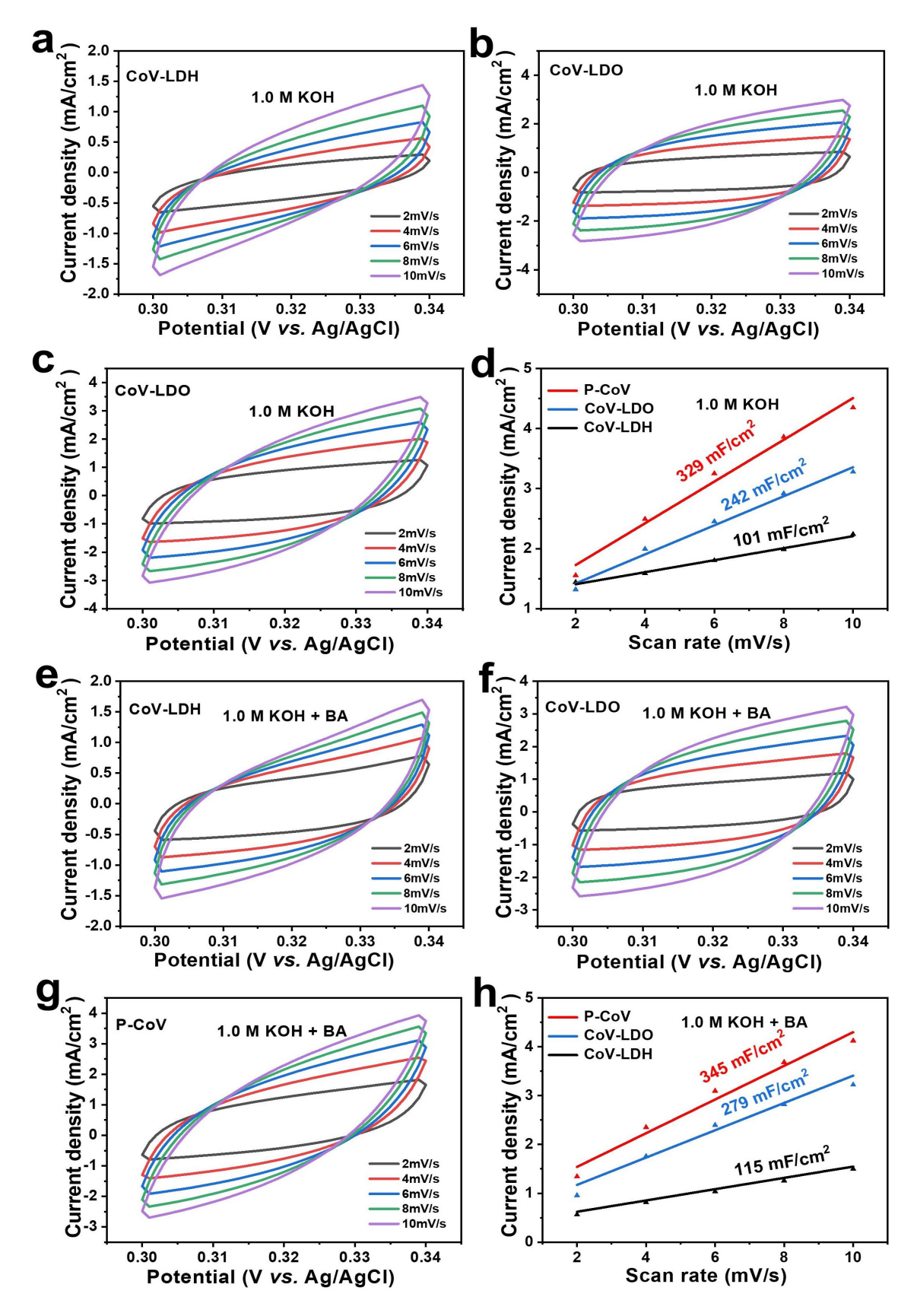


Fig. 4. CV curves of (a) CoV-LDH, (b) CoV-LDO, (c) P-CoV; (d) C_{dl} vales of CoV-LDH, CoV-LDO, and P-CoV in 1.0 M KOH. CV curves of (e) CoV-LDH, (f) CoV-LDO, (g) P-CoV; (h) C_{dl} vales of CoV-LDH, CoV-LDO, and P-CoV in 1.0 M KOH with 10 mM BA.

The incorporation of phosphorus is speculated to yield advantageous electronic environments. These environments would not only help to improve the mobility of electrons, but also quicken the overall catalytic reaction kinetics in both oxidation reactions.

To further analyze the effect of surface area on electrochemical performance, the ECSA of CoV-LDH, CoV-LDO, and P-CoV was estimated based on the C_{dl} derived from CV measurements conducted in the non-Faraday potential region. These tests were completed in both 1 M KOH (Fig. 4a-c) and 1 M KOH with 10 mM BA (Fig. 4e-g) electrolytes under the rates of 2, 4, 6, 8, and 10 mV/s, respectively. The image provides a clear visual representation of the current density of P-CoV, with the highest observed at the same scan rate, followed by CoV-LDO and the lowest at CoV-LDH. The C_{dl} values of CoV-LDH, CoV-LDO, and P-CoV in 1 M KOH (Fig. 4d) were 101 mF/cm², 242 mF/cm² and 329 mF/cm², respectively. Among them, P-CoV possessed the highest C_{dl} value, indicating a larger ECSA and more active centers for OER, which contributes to its superior electrocatalytic activity. In the mixed electrolyte containing BA (Fig. 4h), the C_{dl} values of CoV-LDH, CoV-LDO, and P-CoV were 115 mF/cm², 279 mF/cm² and 345 mF/cm², respectively, following the same trend as observed in pure KOH. Notably, all three samples exhibited higher Cdl values in the presence of BA, suggesting enhanced surface activity and a greater tendency for BA to undergo electrooxidation under these conditions. The combination of high ECSA, low charge transfer resistance, and reduced overpotential underscores the excellent electrocatalytic capability of P-CoV, making it a promising candidate for efficient electrooxidation applications.

Electrocatalytic experiments were completed in 1.0 M KOH with a 10 mM BA electrolyte. BA concentration and electrocatalytic products were quantitatively detected by HPLC. Quantification was conducted via the external standard method by first measuring the peak areas of standard solutions at various known concentrations. Since the peak area changes with concentration in a linear relationship, the concentration of the corresponding product can be analyzed and calculated by referencing the standard calibration curves. HPLC analysis of the standard solutions showed that the retention times of BA, BAD, and BAC were approximately 6.1-6.5 min, 13.4-14.4 min, and 7.9-8.6 min, respectively (Fig. 5a). Calibration curves were established by linear fitting of peak areas against concentration (Fig. 5b-5d). The correlation coefficients of the standard curves of BA and BAC were 0.9993, with minimal Y-intercepts, indicating high linearity and low dilution error in standard solution preparation. In contrast, the calibration curve for BAD exhibited a lower correlation coefficient of 0.9868 and a relatively larger Y-intercept, suggesting some degree of dilution error during standard solution preparation. In addition, the calibration curves showed a consistent increase in peak area with increasing analyte concentration. The peak area reached saturation at a concentration of 10 mM, which was therefore chosen as the initial concentration for the subsequent electrocatalytic product analysis.

In order to investigate the optimal electrocatalytic conditions for maximizing BA conversion a series of single-variable experiments were conducted with subsequent product analysis. The initial conditions were set as: starting potential of 0.5 V, ambient temperature, reaction duration of 9 h, and initial BA concentration of 10 mM. Electrode materials tested included CoV-LDH, CoV-LDO, and P-CoV. Product analysis by HPLC revealed that the P-CoV showed the lowest peak intensity of BA and the highest peak intensity of BAC and BAD among the three catalysts (Fig. 6a), suggesting superior electrocatalytic activity. Quantitative analysis confirmed this observation, with P-CoV achieving a BA conversion of 61.60% and a BAC selectivity of 82.67% (Fig. 6b). As a result, subsequent experiments will use P-CoV as the optimal electrocatalyst.

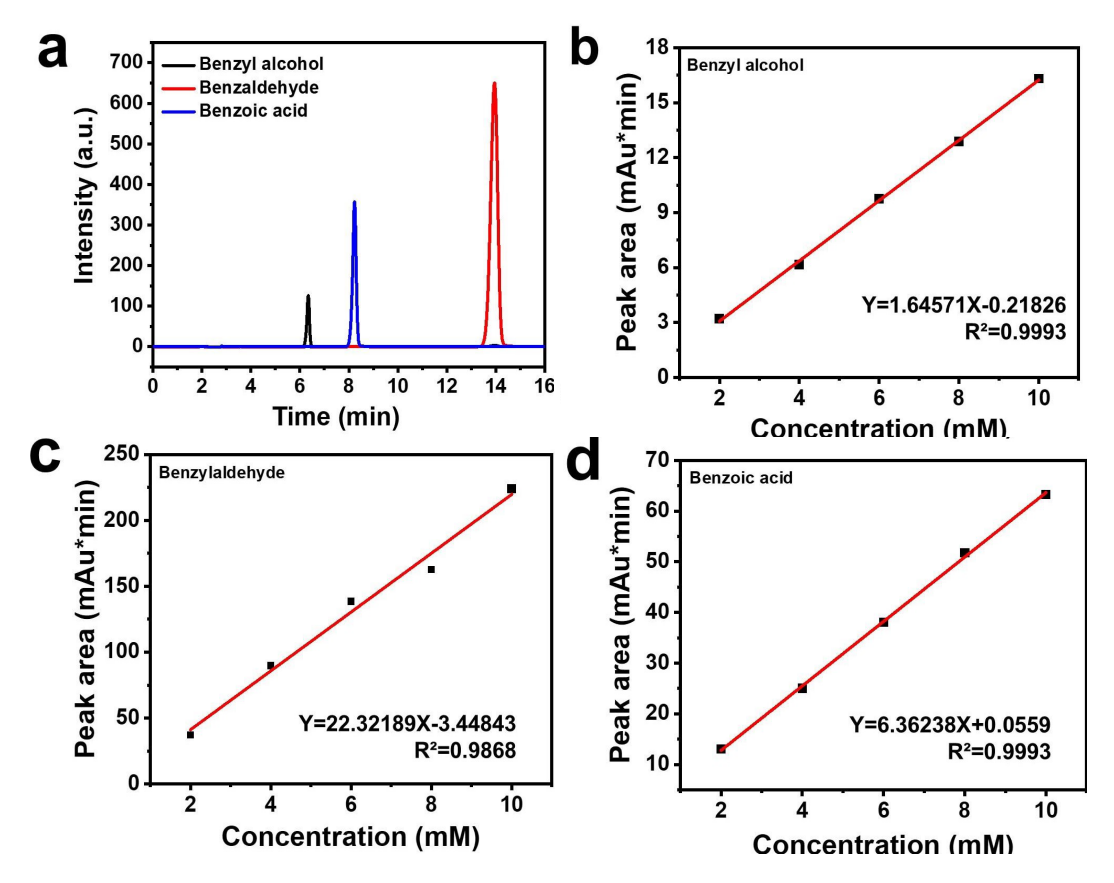


Fig. 5. (a) HPLC spectra of BA, BAC, and BAD; Correlation standard curves of (b) BA, (c) BAC and (d) BAD concentration with liquid phase peak area.

For the purpose of exploring the influence of the applied voltage, the BA oxidation reaction was carried out using P-CoV under varying initial potentials ranging 0.4-0.7 V, while maintaining all other conditions constant. The HPLC chromatograms indicated near-complete BA conversion at 0.7 V, with a dominant BAC peak and a notably low BAD peak (Fig. 6c). The result in Fig. 6d indicated that BA conversion and BAC selectivity all enhanced with the rising of applied potential, whereas BAD selectivity decreased, which was mainly due to the peroxidation of BAD to BAC. Although the highest BA conversion (95.12%) was observed at 0.7 V, this higher potential also entails increased energy consumption and compromised BAD selectivity. A comparison between 0.5 V and 0.6 V revealed that the modest gain in selectivity at 0.6 V does not justify the associated drawbacks. Additionally, higher potentials may induce degradation or delamination of the electrode material, adversely affecting catalyst stability and reusability. Accordingly, 0.5 V was selected as the ideal starting point for subsequent electrocatalytic studies.

Finally, the optimal reaction temperature for electrooxidation of BA was investigated by analyzing the products distribution under various reaction temperatures (RT, 30°C, 40°C, and 50°C) for 9 h with an external potential of 0.5 V using P-CoV as the catalyst and 10 mM BA as the substrate. HPLC analysis (Fig. 6e) showed that at 50°C, the BA conversion was the highest, as evidenced by the minimal residual BA peak and the most intense BAC peak. However, the BAD peak was notably diminished. Quantitative analysis (Fig. 6f) showed a non-linear relationship between temperature and product selectivity: both BAC selectivity and BA conversion initially decreased and then increase with rising temperature, while BAD selectivity exhibited the opposite trend. This behavior is likely due to the overoxidation of BAD to BAC at elevated temperatures. At 40°C, the BA conversion reached 62.96%, which was comparable to that at room temperature (61.60%). However, BAC selectivity was slightly higher at room temperature (82.67%) compared to 40°C (approximately 68%). At 50°C, the BA conversion peaked at 90.04%, while BAC selectivity remained high at 80.21%, slightly lower than at RT. Considering that high conversion and selectivity

can be achieved at room temperature without external heating, which simplifies the reaction setup and reduces energy input, room temperature was identified as the optimal reaction condition.

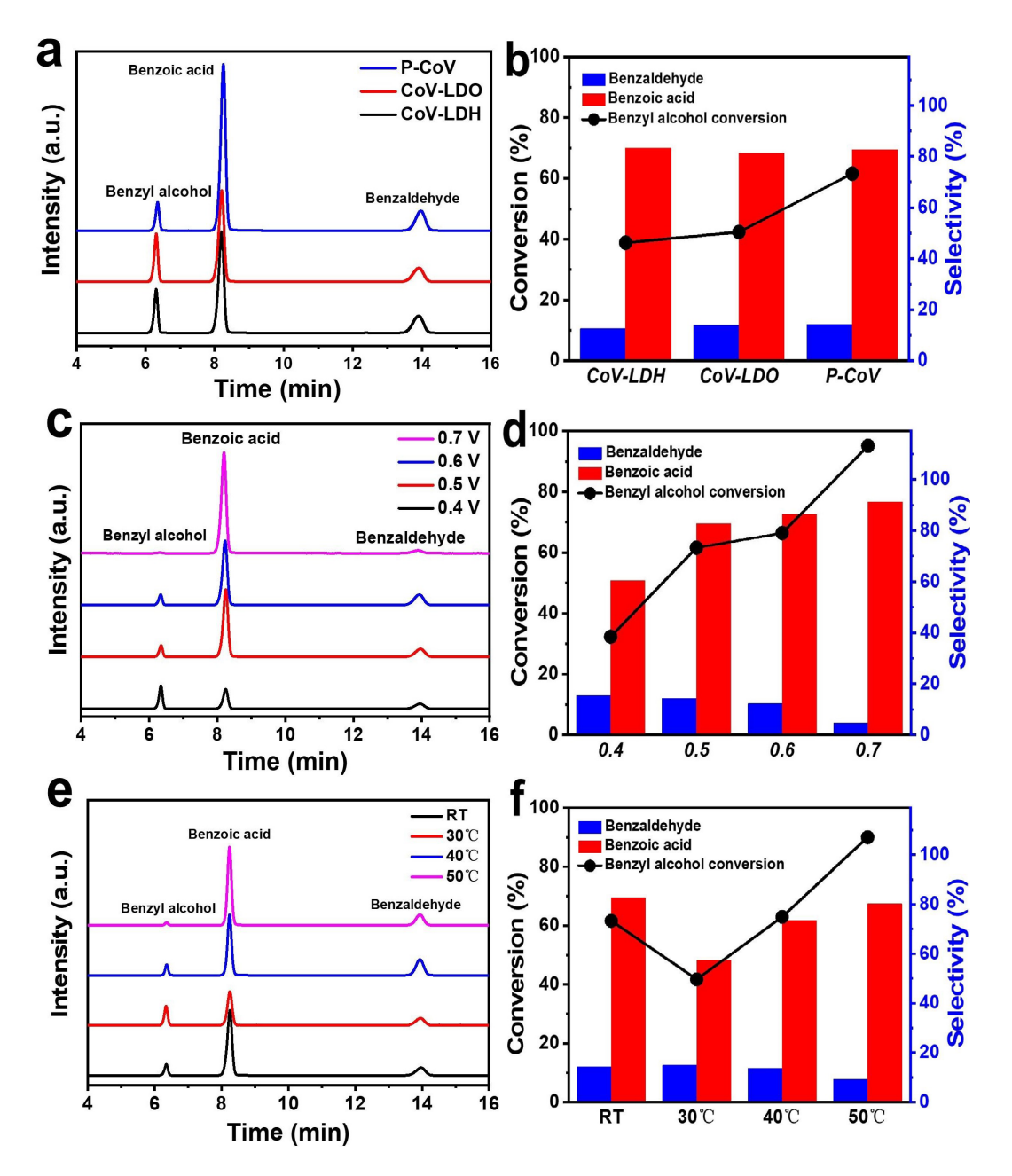


Fig. 6. HPLC spectra of BA, BAC, and BAD under the variable at (a) different catalysts, (c) different onset potentials, and (e) different temperatures; BA conversion and products selectivity after electrocatalysis for 9 h at (b) different catalysts, (d) different onset potentials, and (f) different temperatures.

4. Conclusion

In summary, a cobalt-vanadium bimetallic phosphide (P-CoV) electrocatalyst was successfully synthesized via topological transformation of the CoV-layered double hydroxide (CoV-LDH) through phosphating using NaH₂PO₂. Benefiting from the synergistic effect of bimetallic components, abundant exposed reaction sites, improved electrical conductivity, and enhanced electronic transmission capability, P-CoV demonstrated outstanding electrooxidation of benzyl alcohol (BA) with high selectivity toward benzoic acid (BAC). Notably, Under the optimized

parameters (0.5 V vs. Ag/AgCl, 25°C, 9 h), P-CoV achieved a BA conversion of 61.60% and a BAC selectivity of 82.67%. This study proposes a potential avenue for effective explorations of transition metal phosphide electrocatalysts, offering valuable insights into the discovery of cost-effective and highly effective non-precious metal catalysts for sustainable electrochemical oxidation processes.

Acknowledgements

This project obtained the supports of the Guangxi Natural Science Foundation (No. 2023GXNSFBA026183, No. 2025GXNSFAA069404), and the National Innovation and Entrepreneurship Training Program for college students (No. 202510596029).

References

- [1] Y. Song, M. Yuan, W. Su, D. Guo, X. Chen, G. Sun, W. Zhang, Inorganic Chemistry **61**(19), 7308-7317(2022); http://doi.org/10.1021/acs.inorgchem.2c00082
- [2] J. Qiu, T. Forbes, T. Lin, Chemical Communications **61**(17), 3421-3435(2025); http://doi.org/10.1039/D4CC04822A
- [3] N. Al-Rifai, P. J. Miedziak, M. Morad, M. Sankar, C. Waldron, S. Cattaneo, E. Cao, S. Pattisson, D. Morgan, D. Bethell, G. J. Hutchings, A. Gavriilidis, Industrial & Engineering Chemistry Research **56**(45), 12984-12993(2017); http://doi.org/10.1021/acs.iecr.7b01159
- [4] L. Ming, X.-Y. Wu, S.-S. Wang, W. Wu, C.-Z. Lu, Green Chemistry **23**(19), 7825-7830(2021); http://doi.org/10.1039/D1GC02218K
- [5] L. Liu, N. Li, J. Han, K. Yao, H. Liang, International Journal of Minerals, Metallurgy and Materials **29**(3), 503-512(2022); http://doi.org/10.1007/s12613-021-2352-9
- [6] J. Shi, W. Peng, Y.-F. Yang, B. Li, J. Nie, H. Wan, Y. Li, G.-F. Huang, W. Hu, W.-Q. Huang, Small **19**(30), 2302906(2023); https://doi.org/10.1002/smll.202302906
- [7] A. R. Sugandhi, A. Mohammed, S. V. S. Nair, R. Sreenivasan, New Journal of Chemistry **48**(37), 16278-16288(2024); http://doi.org/10.1039/D4NJ03362K
- [8] X. Xiao, L. Tao, M. Li, X. Lv, D. Huang, X. Jiang, H. Pan, M. Wang, Y. Shen, Chemical Science **9**(7), 1970-1975(2018); http://doi.org/10.1039/C7SC04849A
- [9] S. Wang, S. Chen, C. Wen, L. Dong, C. Tan, B. Li, M. Fan, H. He, Z. Chen, International Journal of Hydrogen Energy **66**, 103-109(2024); http://doi.org/10.1016/j.ijhydene.2024.04.094 [10] L. Lin, M. Chen, L. Wu, Materials Chemistry Frontiers **5**(1), 375-385(2021); http://doi.org/10.1039/D0QM00635A
- [11] P. Wei, X. Li, Z. He, Z. Li, X. Zhang, X. Sun, Q. Li, H. Yang, J. Han, Y. Huang, Applied Catalysis B: Environmental **299**, 120657(2021); https://doi.org/10.1016/j.apcatb.2021.120657
- [12] V. Jain, Y. Bonita, A. Brown, A. Taconi, J. C. Hicks, N. Rai, Catalysis Science & Technology **8**(16), 4083-4096(2018); http://doi.org/10.1039/C8CY00977E
- [13] S. Liu, S. Song, Y. Feng, Catalysis Letters **155**(2), 88(2025); http://doi.org/10.1007/s10562-024-04894-6
- [14] P. Li, H. C. Zeng, Journal of Materials Chemistry A **6**(5), 2231-2238(2018); http://doi.org/10.1039/C7TA10665C
- [15] G. Li, Y. Xu, H. Pan, X. Xie, R. Chen, D. Wu, L. Wang, Journal of Materials Chemistry A **10**(12), 6748-6761(2022); http://doi.org/10.1039/D1TA09412B
- [16] L. Wang, N. Gong, Z. Zhou, W. Peng, Y. Li, F. Zhang, X. Fan, International Journal of Hydrogen Energy 47(42), 18305-18313(2022); http://doi.org/10.1016/j.ijhydene.2022.04.024
- [17] J. Zhao, K. Li, H. She, Y. Zhang, J. Huang, L. Wang, F. Cheng, Q. Wang, Journal of Colloid and Interface Science **649**, 416-425(2023); https://doi.org/10.1016/j.jcis.2023.06.112
- [18] Y.-J. Li, L.-D. Xue, Y.-D. Zhang, L.-L. Zhang, G.-W. Chu, B.-C. Sun, J.-F. Chen, AIChE Journal **69**(3), e18006(2023); http://doi.org/10.1002/aic.18006
- [19] M. Liu, M. Zhong, H. Li, L. Piao, W. Wang, ChemPlusChem **80**(4), 688-696(2015); https://doi.org/10.1002/cplu.201402368

- [20] Y. Xu, H. Liu, Y. Wu, Q. Wu, C. Li, X. Wang, H. Qin, A. Qin, L. Wang, Chemnanomat 9(12), e202300414(2023); http://doi.org/10.1002/cnma.202300414
- [21] W. Ye, C. He, M. Asim Mushtaq, K. Lin, X. Xing, European Journal of Inorganic Chemistry **2022**(26), e202200325(2022); https://doi.org/10.1002/ejic.202200325
- [22] L. V. Quispe-Garrido, I. E. Monje, E. O. López, J. M. Gonçalves, C. S. Martins, G. Á. Planes, J. G. Ruiz-Montoya, A. M. Baena-Moncada, ACS Omega 7(48), 43522-43530(2022); http://doi.org/10.1021/acsomega.2c04126